



Mapping humidity-dependent mechanical properties of a single cellulose fibre

Julia Auernhammer · Tom Keil · Binbin Lin · Jan-Lukas Schäfer ·
Bai-Xiang Xu · Markus Biesalski · Robert W. Stark

Received: 14 September 2020 / Accepted: 30 June 2021 / Published online: 14 July 2021
© The Author(s) 2021

Abstract Modelling of single cellulose fibres is usually performed by assuming homogenous properties, such as strength and Young's modulus, for the whole fibre. Additionally, the inhomogeneity in size and swelling behaviour along the fibre is often disregarded. For better numerical models, a more detailed characterisation of the fibre is required. Herein, we report a method based on atomic force microscopy to map these properties along the fibre. A fibre was mechanically characterised by static colloidal probe AFM measurements along the longitudinal direction of the fibre. Thus, the contact stress and strain at each loading point could be extracted. Stress–strain curves were obtained along the fibre.

Additionally, mechanical properties such as adhesion or dissipation were mapped. Local variations of the effective fibre radius were recorded via confocal laser scanning microscopy. Scanning electron microscopy measurements revealed the local macroscopic fibril orientation and provided an overview of the fibre topography. By combining these data, regions along the fibre with higher adhesion, dissipation, bending ability and strain or differences in the contact stress when increasing the relative humidity could be identified. This combined approach allows for one to obtain a detailed picture of the mechanical properties of single fibres.

Supplementary Information The online version contains supplementary material available at <https://doi.org/10.1007/s10570-021-04058-4>.

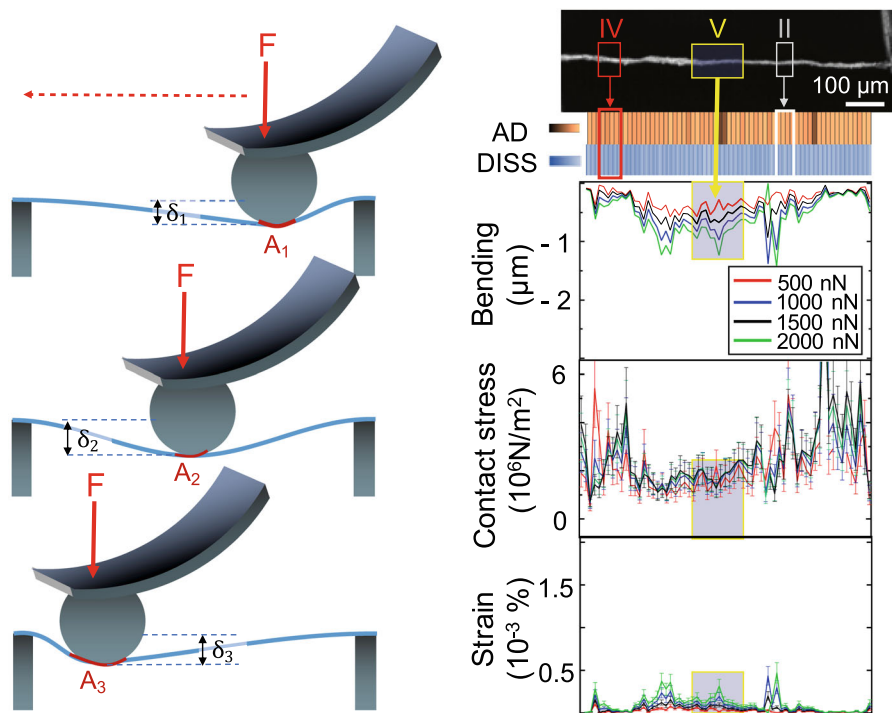
J. Auernhammer · R. W. Stark (✉)
Institute of Materials Science, Physics of Surfaces,
Technical University of Darmstadt, Alarich-Weiss-Str. 16,
64287 Darmstadt, Germany
e-mail: stark@pos.tu-darmstadt.de

T. Keil
Institute of Materials Science, Physical Metallurgy,
Technical University of Darmstadt, Alarich-Weiss-Str. 2,
64287 Darmstadt, Germany

B. Lin · B.-X. Xu
Institute of Materials Science, Technical University of
Darmstadt, Mechanics of Functional Materials, Alarich-
Weiss-Str. 16, 64287 Darmstadt, Germany

J.-L. Schäfer · M. Biesalski
Department of Chemistry, Macromolecular Chemistry and
Paper Chemistry, and Center of Smart Interfaces (CSI),
Technical University of Darmstadt, Petersenstraße 22,
64287 Darmstadt, Germany

Graphic abstract



Keywords Cellulose · Single Fibre Strength · Scanning Electron Microscopy · Confocal Laser Scanning Microscopy · Atomic Force Microscopy · Colloidal Probe

Introduction

Cellulose-based papers have promising applications in areas such as electronics, sensor technology, microfluidics, and medicine (Bump, 2015; Delaney et al. 2011; Hayes and Feenstra 2003; Liana et al. 2012; Ruettiger, 2016). However, before paper can be used as a substrate material for these technologies, an understanding of how the mechanical properties depend on the structure and variations and inhomogeneities of single cellulosic fibres must be improved. Cellulose is a naturally occurring material that is abundant and renewable. It is the most important raw material in the paper-making industry. In pulping and paper making, the flexibility of a single fibre plays an important role. Flexibility is responsible for quality during sheet formation and production of types of papers (Persson

et al. 2013). To control this process, characterisation of the processed fibres is important.

Young's modulus is a mechanical parameter that can be used to describe a single fibre. In tensile tests, a Young's modulus between 20 and 80 GPa was measured for single fibres (Groom et al. 2002; Jayne 1959; Lorbach et al. 2014; Page et al. 1977). Via an AFM-based three-point bending test, the Young's modulus of a single pine fibre could be quantified to 24.4 GPa (Fernando et al. 2017). Large variations in the Young's moduli of different fibres are due to the different types of fibres, such as earlywood vs latewood, and botanical aspects, such as cell wall thickness or fibre width. Additionally, the microfibril angle plays an important role in the single fibre strength. A small microfibril angle was shown to be correlated with a high longitudinal elastic modulus (Müssig 2010).

The parameter of bending stiffness is defined as the Young's modulus multiplied by the second moment of inertia (Samuelsson 1963). The bending stiffness of dry earlywood fibres was tested to be $3.1 \cdot 10^{-5} \text{ N}^{-1} \text{ m}^{-2}$, and that of latewood was tested to be $1.5 \cdot 10^{-4} \text{ N}^{-1} \text{ m}^{-2}$. When wetting the fibre, the

bending stiffness was reduced to $0.9 \cdot 10^{-5} \text{ N}^{-1} \text{ m}^{-2}$ for earlywood and to $2.6 \cdot 10^{-5} \text{ N}^{-1} \text{ m}^{-2}$ for latewood (Schniewind et al. 1966). Flexibility is another relevant mechanical parameter that characterises single fibres. It is defined as the reciprocal bending stiffness (Yan and Li 2008). Flexibility can be characterised by flowing the fibres between two rotating cylinders (Arlov AP 1958; Forgacs OL 1958) or obtained via AFM-based methods. One method is to mount a single fibre over a trench and test the flexibility of the fibre with a colloidal probe attached to the cantilever (Navaranjan et al. 2008). Another approach is to attach the fibre at one end only. At the free end, the cantilever tests the flexibility via static force-distance curves. Here, bleached softwood fibres exhibited a flexibility of $4\text{--}28 \cdot 10^{12} \text{ N}^{-1} \text{ m}^{-2}$, and in TMP fibres, the flexibility was one order of magnitude lower (Pettersson et al. 2017). These examples illustrate the drastic effect of humidity on fibre mechanics.

Thus, the influence of humid air or water on the mechanical properties of natural fibres is an important topic to be addressed in the application of cellulose-based materials. The impact of relative humidity (RH) on the elastic modulus, stiffness, or strength has been investigated by various authors (Ganser et al. 2015; Placet et al. 2012; Salmen and Back 1980). With an AFM-based indentation method, it was possible to test the mechanical properties of wet cellulose and estimate the Young's modulus, which was in the kPa range (Hellwig et al. 2018). Likewise, nano mechanical mapping by AFM indicated a decrease of the DMT modulus in a humid environment (Auernhammer, 2021). Additionally, the viscoelastic properties of pulp fibres could be investigated with AFM. In these experiments, the RH was varied from 10 to 75%, and the elastic modulus and viscosity of the fibre were recorded. The elastic moduli decreased by a factor of ten, and the viscosity decreased by a factor of ten to 20. The fibres exhibited a decrease in the elastic moduli by a factor of 100 after water immersion, and the viscosity decreased by at least three orders of magnitude (Czibula et al. 2019). Further AFM-based colloidal probe measurements on cellulose were performed on gel beads made of cellulose to show the impact on mechanical properties in the wet state (Hellwig et al. 2017). Additionally, the breaking load of a single fibre depending on the RH could be determined, whereas the breaking load decreased with increasing RH (Jajcinovic et al. 2018).

Since cellulose fibres are natural fibres with a hierarchical structure, one must account for the variability in the mechanical parameters within and along the longitudinal direction of the fibre. Earlier, the inhomogeneous swelling behaviour of cellulose fibres was reported (Fidale et al. 2008; Placet et al. 2012). The swelling process of cellulose fibres is determined by the crystallinity, the degree of polymerization, the degree of fibrillation and the pore size (Buschlediller and Zeronian 1992; El Seoud et al. 2008; Fidale et al. 2008; Mantanis et al. 1995). Additionally, variability in cross-sectional areas within the fibre must be considered, as pointed out by (Biswas et al. 2013) and (Chard et al. 2013).

To establish mechanical models of fibres and fibre networks that account for the intra-fibre variability in mechanical parameters, it is essential to locally characterize fibres (Lin 2020). In the following paper, we report an AFM-based method to map the strength, flexibility, and mechanical properties of single cellulose fibres depending on relative humidity and based on different sections of the fibre. Other methods, such as the three-point bending test, are often based on the assumption of a constant cross section along the longitudinal direction of the fibre. However, this assumption might be slightly too simple to yield a good mechanical representation of cellulosic fibres in the dry state and even less in the wet state. To account for the variation in the cross section, we characterised the geometrical and mechanical properties of cellulose fibres along their longitudinal direction section by section.

First, we observed the behaviour of the local fibre surface radius of the fibre along its longitudinal direction via confocal laser scanning microscopy. The changes in the local fibre surface radius were considered for each fibre section. Then, we generate static force-distance curves via atomic force microscopy with a colloidal probe to test the mechanical properties at every local loading point of the fibre. The local topography was recorded by scanning electron microscopy measurements. A cotton linter fibre, which consists of 95% cellulose, served as the model system (Mather and Wardman 2015; Young and Rowell 1986), and the results indicate that the mechanical properties of the fibres strongly varied along the longitudinal direction of the fibre, particularly in a humid environment.

Materials and methods

Materials

Cellulose fibres were manually extracted from a cotton linter paper sheet that was prepared according to DIN 54,358 and ISO 5269/2 (Rapid-Köthen process). Further information on the fibre is given in table S1. The extracted fibre was mounted on a 3D printed sample holder, which supplied a fixed trench distance L of 1 mm between the two attachment points. Thus, the fibre under test was freely suspended and fully exposed to the humid environment, which minimized the influences of a substrate or other connecting fibre bonds. The set up was similar to that of other authors (Schmied et al. 2013, 2012). The glue did not penetrate the fibre, as shown in Figure S1.

Methods

Confocal laser scanning microscopy (CLSM) measurements were conducted to estimate the local fibre surface curvature radius R_{Fibre} . With AFM, we could detect the local bending δ , adhesion, and dissipation to complete the mechanical property image with the calculated local occurring contact stress σ (unit: N/m^2) and strain ε (unit: %) at each bending point. For the calculation of contact stress σ , the R_{Fibre} from the CLSM measurements were used. Regions with notably unique mechanical behaviour or an increase in R_{Fibre} were investigated and related to the local macroscopic fibril orientation on the fibre surface, which was identified with SEM. In CLSM and AFM measurements, the relative humidity (RH) was varied. For every RH step, the fibre was measured first at the CLSM in a climate chamber and was then moved to the AFM and put inside the climate chamber for uniform conditioning and reliable results as described in the following sections. After measuring at a certain RH, the sample was moved back to the CLSM and the RH was increased.

To assess the repeatability of the measurement technique the fibre was exposed to two cycles RH variation. After the first cycle the fibre was allowed to dry for 6 days and then the measurements of the second humidity cycle were carried out.

Confocal laser scanning microscopy

A VK-8710 (Keyence, Osaka, Japan) CLSM instrument was used to investigate the local fibre surface curvature radius R_{Fibre} . The local surface curvature is a parameter which represents the surface curvature of the fibre at the contact area between the colloidal probe and the fibre as illustrated in Fig. 1. Note, that R_{Fibre} is an estimate for the local curvature at the point of contact between colloidal probe and fibre and thus does not parameterize the fibre cross section. The parameter R_{Fibre} was used to estimate the contact stiffness from the colloidal probe measurements.

To this end, the fibre was placed into a climate chamber, where the RH was set at 2%, 40%, 75%, and 90%. The fibre was exposed to the RH for 45 min before measuring. Additionally, each experiment at the adjusted RH took at least 30 min in total. Thus, the measurements were carried while the fibres were not yet fully equilibrated. To reach a full adsorption/desorption equilibrium from the gas phase, an “exposure time” of at least twelve hours (Jajcinovic et al. 2018) would have been necessary. However, to ensure consistency between CLSM and AFM measurements and to avoid drift problems in AFM, we defined 45 min of “exposure time” as a feasible compromise to balance effects from instrumental drift and slow swelling processes.

The change of the local surface curvature radius of the fibre was analysed using the VK analyser software from Keyence (Osaka, Japan). First, the data were noise corrected. Then, cross sections were measured along the longitudinal direction of the fibre to estimate the fibre surface curvature radius R_{Fibre} at each loading point. A representative cross section is shown in Fig. 1, and the corresponding recorded three-dimensional fibre images are shown in Figure S2. For every

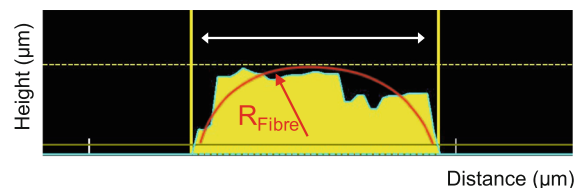


Fig. 1 A representative CLSM measurement of the cross section of the fibre surface of a loading point of the fibre. The estimated fibre surface curvature radius is indicated in red. Note that R_{Fibre} parameterises a local curvature and not the cross section of the fibre

loading point, such a cross section was drawn. The change in R_{Fibre} with increasing RH was normalised to the R_{Fibre} of 2% RH and plotted against the RH. The local investigated fibre surface curvature radius spot R_{Fibre} is needed to calculate the contact area A (Eq. 15) between the colloidal probe and fibre.

Furthermore, regions of homogeneously varying behaviour were identified along the fibre diameter. At every loading point, the R_{Fibre} was analysed for every RH. Then, the change in R_{Fibre} at every loading point with varying RH was noted. The regions of interest (ROIs) were defined as having a similar, normalised increase in R_{Fibre} when varying the RH. The ROIs were then subjected to SEM for further investigation.

The fibre was fixed at both ends to minimise fibre twisting. For that reason, we did not observe a strong twisting phenomenon within the evaluation of R_{Fibre} with different RHs.

Atomic force microscopy

A Dimension ICON (Bruker, Santa Barbara, USA) was used to measure static force-distance curves along the longitudinal direction of the fibre with a colloidal probe. The cantilever (RTESPA 525, Bruker, Santa Barbara, USA) with a nominal spring constant of 200 N/m (measured via thermal noise method (Butt and Jaschke 1995)) was modified with a 50 μm diameter SiO_2 colloidal probe (Glass-beads, Kisker Biotech GmbH & Co. KG, Steinfurt, Germany). The deflection sensitivity of the cantilever (invOLS) was calibrated by performing a force-distance curve on a hard sapphire surface. All AFM experiments were performed in a climate chamber. Hence, it was possible to vary the relative humidity (RH) during the experiments. The chosen RH values were 2%, 40%, 75%, and 90%. As the RH was adjusted, the fibre was exposed to the environment for 45 min before starting the measurements. Force-distance curves were acquired every 5 μm along the freely suspended fibre in longitudinal direction.

The fibre was fixed at both ends to strain the fibre and prevent twisting of the fibre as the force was applied. Twisting and sideways slippage of the colloidal probe during force curve measurement was investigated in preliminary experiments (data not shown). By trial and error, a colloidal probe diameter of 50 μm turned out to limit slippage on the fibre under test. A step size of 5 μm in the axial direction was set

and automatically controlled by AFM software. The lateral position of the colloidal probe was corrected manually based on the camera image. Thus, the scan along the fibre was aligned stepwise along the longitudinal direction of the fibre (Fig. 2). Additionally, fibre bending by the colloidal probe was monitored with the camera image to ensure consistent AFM data. Finally, the recorded force-distance curves were inspected for obvious features of a slipped colloidal probe. In the case of slippage, the probe was repositioned, and the measurement was repeated.

Via cantilever calibration and the deflection sensitivity, the recorded deflection-piezo position curves were transferred to force-distance curves. A schematic force-distance curve is shown in Fig. 3a). The peak force setpoint was 2100 nN. The baseline was corrected with a linear fit function to the initial flat region. The contact point was defined with MATLAB (The MathWorks, Inc. Natick, Massachusetts, USA) toolbox code from Bruker. The method first determines the contact point of the curve. The code and its explanation are provided in the Supplementary Information. In general, finding the contact point in force-separation curves reliably is difficult. Various strategies to automatically determine the contact point have been reported (Benitez et al. 2013; Gavara 2016; Lin et al. 2007; Rudoy et al. 2010). Our method is designed to identify the contact point by a sharp transition between the out-of contact and in-contact signal. If there is a smooth transition between both regimes, the estimate for the contact point might be less accurate. We recorded 512 points per curve (512 per trace and 512 per retrace). We assume an error of 20% in the bending data to account for the potential measurement errors.

Mechanical properties such as adhesion and energy dissipation were extracted from the force-distance curve, as illustrated in Fig. 3a. The adhesion force was identified as the lowest point in the retrace curve (red curve in Fig. 3a), and the dissipation was defined as the integrated area between the trace and retrace curves (blue and red curves in Fig. 3a). In Fig. 3b), a schematic force-bending curve is displayed. To transform the force-distance curves into force-bending curves, the MATLAB code identifies the contact point in the trace curve (blue in Figs. 3 and 4) and sets this point as zero (offset). For the force-distance curve, the offset is in the origin of the curve (cf. position of zero value in Fig. 3a and 3b). From the data, the fibre

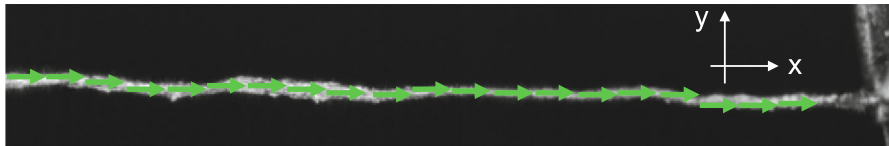


Fig. 2 Schematics of the section-wise scanning process along the longitudinal direction of the fibre. At every section, the scanning trajectory was realigned to the fibre axis

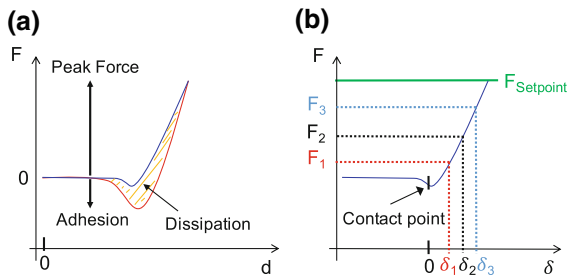


Fig. 3 **a** Schematic force-distance curve with extracted mechanical properties. **b** Force-bending curve with visualization of multiple virtual setpoint forces F

bending δ can be read out for various forces from the data to create virtual height maps for these forces, as schematically illustrated in Fig. 3b. For mapping, we determined the fibre bending for 500 nN, 1000 nN, 1500 nN, and 2000 nN. This allows for one to easily detect a potentially nonlinear local response of the fibre.

This non-linearity is shown in Fig. 4a–d with representative force-bending curves at different RHs. The curves clearly show the nonlinear force-bending relationship. Thus, the bending for different applied forces cannot be easily estimated, as seen in the sketch (Fig. 3b). Due to piezo hysteresis or thermal drift trace

(blue) and retrace (retrace) curves did not merge not in the contact point region (4b–d).

In contrast to the conventional three-point bending test (Fig. 5a), where the specimen is bent only at the centre, we performed a test along the longitudinal direction of the fibre every 5 μm in a scanning three-point bending test (Fig. 5c). In conventional three-point bending testing, the second moment of inertia

$$I = \frac{\pi}{4} \cdot (r_2^4 - r_1^4) \quad (1)$$

is a critical parameter that must be homogenized along the fibre to obtain Young's modulus

$$E = \frac{F \cdot L^3}{192 \cdot \delta \cdot I} \quad (2)$$

The calculation of Young's modulus via the conventional three-point bending test includes the applied force F , the trench length L , the bending distance δ , and the second moment of inertia I . The second moment of inertia I includes the inner and outer radii (r_1 and r_2) of a schematic circular fibre, as shown in the cross section in Fig. 4b). Since a cotton linter fibre is a natural fibre, the dimensions along the fibre cannot be modelled using a single value for the cross section. To circumvent this problem, we performed many bending tests and scanned along the longitudinal

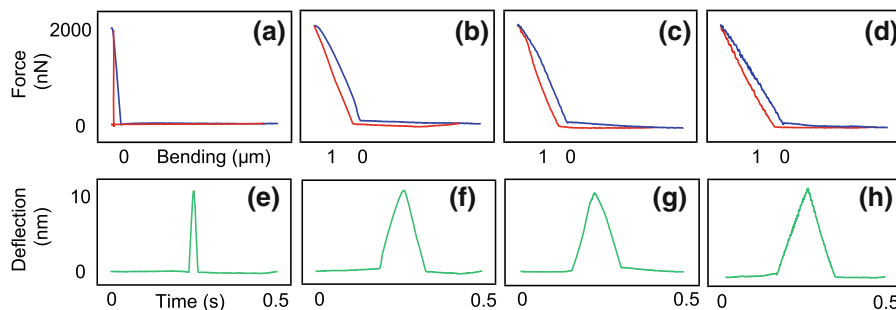


Fig. 4 **a–d** Force-bending curves measured at different RHs. The curves from loading point #15 (from left to right in Fig. 9) are shown. In blue: trace curve, in red: retrace curve. The force-bending curves exhibited a slightly non-linear force-bending

relationship. Therefore, bending was read out at different forces to create a map which highlights strongly non-linear regions. **e–h**) Force–time plots of the corresponding force-bending curves at the different RHs

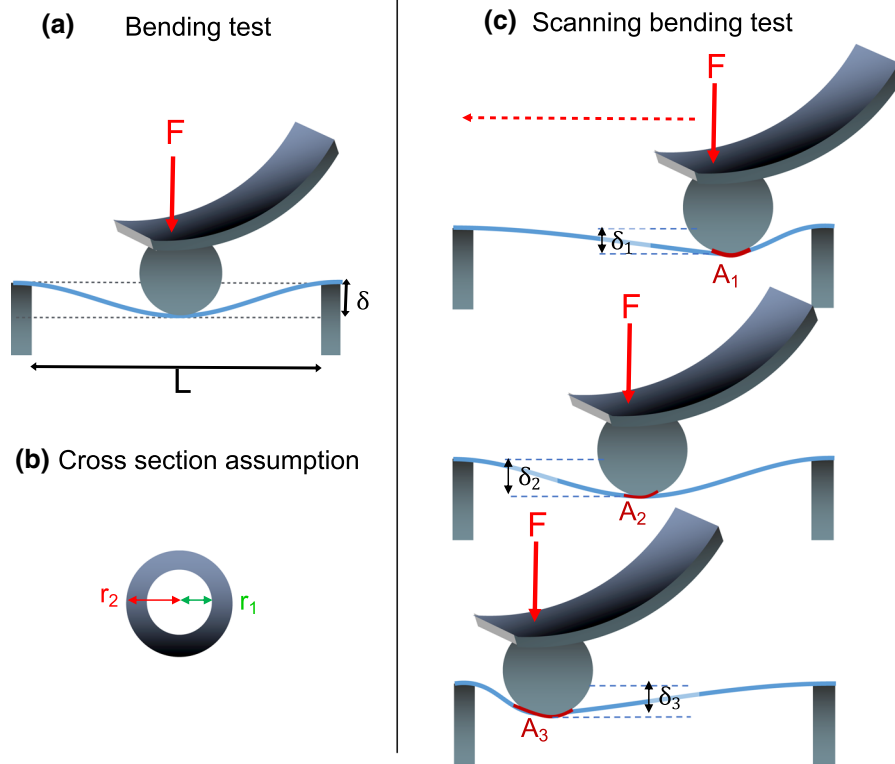


Fig. 5 **a** Schematic of a conventional three-point bending test. **b** Cross section of a fibre and the corresponding equations for a three-point bending test. **c** Principle of a scanning three-point bending test

direction of specimen to test and determine the mechanical properties. We were able to detect the local bending δ of the fibre via AFM from the force curves and could, therefore, study the bending behaviour of the fibre at different applied forces. In addition to the local adhesion, dissipation, and bending ability along the longitudinal direction of the fibre, we completed the mechanical property imaging with the local stress:

$$\sigma = \frac{3F}{2A}, \tag{3}$$

and strain

$$\varepsilon = \frac{\Delta L}{L} \tag{4}$$

for each loading point.

The stress was obtained by dividing the applied force F by the contact area A of the colloidal probe and fibre surface multiplied by 3/2 as the contact area exhibits an elliptical shape. The strain is calculated as the elongation ΔL divided by the trench length L . The

estimation of the variables contact area A and elongation ΔL is described in the following.

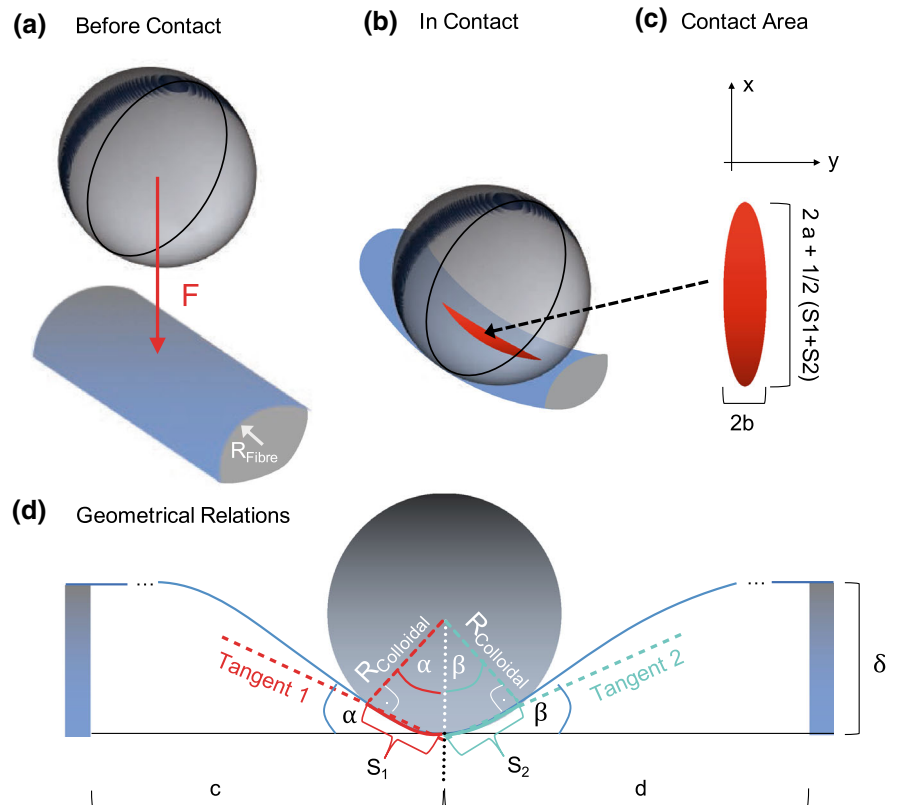
Estimation of contact area A and elongation ΔL

The area A of contact between the colloidal probe and the fibre could not be measured directly. Thus, this parameter had to be estimated to determine the contact stress (Eq. 3). To simplify the model, we assume that rough features at the fibre surface are compressed i.e. that there is a (nearly) conformal contact between probe and fibre.

The contact mechanics of this problem is similar to the contact mechanics of a sphere pressing into a curved surface of a cylinder as illustrated in Fig. 6a, b. The contact areas has an elliptical shape, with the major axis a and the minor axis b . Following (Barber et al. 2018) the major axis a can be calculated as:

$$a = \left(\frac{3F[K(e) - E(e)]}{2\pi e^2 E^* P} \right)^{\frac{1}{3}} \tag{5}$$

Fig. 6 Schematics of the contact mechanics between the colloidal probe and the fibre. **a** Before contact and **b** in contact. The elliptical contact area is illustrated in **(c)**. In **(d)** the geometrical relations between the colloidal probe and the fibre are shown



and the minor axis b as

$$b = a\sqrt{1 - e^2} \quad (6)$$

Here, $K(e)$ is the complete elliptic integral of the first kind, $E(e)$ the complete elliptic integral of the second kind, e the eccentricity, E^* the reduced elastic modulus, and P the principal curvature. As the eccentricity is a function of the profiles of the contacting surfaces, it varies with the different radii along the fibre axis. Thus, the elliptical integrals $K(e)$ and $E(e)$ also vary along the fibre axis. All values are extracted from the diagrams given in (Barber et al. 2018) in chapter 3. For more information see SI chapter “3. Strategy for calculation the eccentricity”.

The reduced elastic modulus E^* is given by

$$\frac{1}{E^*} = \frac{1 - \nu_{Colloidal}^2}{E_{Colloidal}} + \frac{1 - \nu_{Fibre}^2}{E_{Fibre}} \quad (7)$$

The elastic modulus of the SiO_2 colloidal probe ($E_{Colloidal}$) is 35 GPa (AZoMaterials 2020). The elastic modulus of the fibre was determined as the DMT modulus (Derjaguin et al. 1975) of the fibre surface.

The DMT modulus was mapped with a sharp cantilever (Scan Asyst Fluid +, Bruker, Santa Barbara, USA) in PeakForce tapping mode with a force constant of 1.1 N/m, PeakForce Setpoint of 10 nN, and amplitude of 300 nm. Representative DMT modulus maps are shown in figure S5. The DMT modulus was 60 GPa for 2% RH, 21 GPa for 40% RH, 2 GPa for 75% RH and 0.5 GPa for 90% RH. The Poisson’s ratio $\nu_{Colloidal}$ was defined as 0.5, and the Poisson’s ratio ν_{Fibre} was defined as 0.3. The radius of the colloidal probe $R_{Colloidal}$ was 25 μm . The local fibre curvature surface radius R_{Fibre} was recorded via CLSM at every loading point.

To calculate the total contact area A , we assume that the major axis of the ellipse shaped contact area $2a$ is increased by $\frac{1}{2}$ of the arc length of $S_1 + S_2$ due to the bending of the fibre (Fig. 6c). Thus, the contact area is approximated as

$$A = \pi \cdot \left(a + \left(\frac{S_1 + S_2}{4} \right) \right) \cdot b. \quad (8)$$

The geometrical relations of the sphere bending the fibre are shown in Fig. 6d. The model assumes tangents, displayed in dashed red and turquoise, in arc lengths S_1 and S_2 of the fibre and the colloidal probe with occurring angles α and β . Via geometric laws, the same angles are also present between the radius $R_{Colloidal}$ and the white dashed middle line. Variables c and d display the segment lengths to the fixed end of the fibre and present loading point.

The tangents 1 and 2 are defines as:

$$\text{Tangent1} = \sqrt{\delta^2 + c^2} \quad (9)$$

and

$$\text{Tangent 2} = \sqrt{\delta^2 + d^2}. \quad (10)$$

The angles α and β are calculated as:

$$\tan(\alpha) = \frac{\delta}{c} \quad (11)$$

and

$$\tan(\beta) = \frac{\delta}{d}. \quad (12)$$

Therefore, the arc lengths S_1 and S_2 can be defined as

$$S_1 = R_{Colloidal} \cdot \alpha \quad (13)$$

and

$$S_2 = R_{Colloidal} \cdot \beta \quad (14)$$

With the calculated contact area A , the contact stress σ as defined in Eq. 3 can be calculated.

We assume a linear elastic Hertzian contact mechanic and neglect the viscoelastic parts. The viscoelastic behaviour is a time dependent phenomenon. As illustrated in Fig. 4e–h) the fibre was bent only 0.5 s in total at each point of measurement. The force peak at 0.25 s in the time series exhibited hysteretic forces due to adhesion but was otherwise symmetric, which indicates that there were only small contributions from time depending forces (viscoelastic behaviour). This is compatible with literature data, where storage and loss modulus of cellulose fibres were investigated via Brillouin spectroscopy (Elsayad, 2020). The authors concluded that loss modulus (viscous behaviour) was much (25 times) smaller than the storage modulus (elastic behaviour). Thus, it

seems reasonable to neglect the viscous contributions in our simplified contact mechanical model.

Many simplifying assumptions had to be made in the model. Our contact model assumes a conformal contact between colloidal probe and fibre and a homogeneous fibre material. Another error source can be the addition of the arc length $S_1 + S_2$ to the major axis of the elliptical shaped contact area. Additionally, the contact area could also be increased due to the bending in the minor axis $2b$ of the elliptical shaped contact area. Thus, it seems reasonable to assume a rather large error for the estimated contact area A on the order of at least 30%.

To determine the strain along the longitudinal direction of the fibre, elongation ΔL must also be estimated (see Eq. 4). Often, the elongated bending length is determined based on a Euler–Bernoulli beam. However, this approach requires homogeneous parameters, and for a fibre, such homogenization is questionable. Thus, we limited bending to small values, and the maximum fibre bending δ was approximately 2 μm , which is rather small compared to the trench length $L = 1 \text{ mm}$. Thus, the elongation could be estimated from simple geometrical assumptions with:

$$\Delta L = \text{Tangent1} + \text{Tangent2} \quad (15)$$

as illustrated in Fig. 7. We assume an error of 25% of the strain due to the geometrical assumptions.

Scanning electron microscopy

The individual fibre topography was analysed using a scanning electron microscope (SEM) (MIRA3, TESCAN, Brno, Czech Republic) in secondary electron (SE) imaging mode at a low acceleration voltage (3 kV).

Results and discussion

In the following, we first discuss how the radius of the fibre surface curvature R_{Fibre} was measured with CLSM and evolved with increasing RH. Then, by combining CLSM and AFM colloidal probe bending measurements, we developed a mechanical image of a single fibre and related the mechanical behaviour and the increase in R_{Fibre} for each ROI.

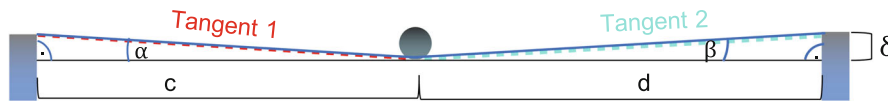


Fig. 7 Schematics of the calculation of the elongation ΔL

Fibre geometry

CLSM measurements were used to measure the change of the paper fibre surface curvature radius R_{Fibre} . These results were used to estimate the contact area A of the colloidal probe and the fibre to determine the contact stress σ . Figure 8a shows a CLSM image of the fibre. The coloured boxes indicate regions of interest, ROIs, as they were used for CLSM and SEM characterization. The ROIs were defined as regions with similar normalised change in R_{Fibre} in a humid environment. In Fig. 8b, the normalised change in R_{Fibre} of the framed ROIs is displayed over the RH in %. The change in R_{Fibre} was normalised by the value of R_{Fibre} at 2% RH in each ROI.

As shown in Fig. 8, the changing behaviour of the surface curvature radius of a natural paper fibre is inhomogeneous along the fibre diameter, as indicated with different ROIs. There is general agreement that cellulose fibres with different degrees of polymerization, cellulose contents, crystallinity, and degrees of

fibrillation are expected to exhibit different degrees of swelling (Buschlediller and Zeronian 1992; El Seoud et al. 2008; Fidale et al. 2008; Mantanis et al. 1995). The increase in R_{Fibre} could origin from fibre swelling or e.g. from fibre twisting. We tried to minimise fibre twisting with the fixed end of the fibre in our set up and did not observe this phenomenon in a strong way, but it cannot be excluded.

Three ROIs (I, II and III) were investigated in more detail. The corresponding SE images of the discussed ROIs are shown in Fig. 9. ROI I (light orange) in Fig. 8a increased to a normalised change in R_{Fibre} of 1.72 ± 0.05 when increasing the RH to 40%. When increasing the RH to 75% and 90%, the R_{Fibre} only slightly increased. The behaviour in ROI II (grey) was different. The changing in R_{Fibre} was much lower until an R_{Fibre} of 1.31 ± 0.09 was reached at 90% RH. In ROI III (green), there was little difference between the radii at 75% and 90% with a normalised change of 1.25 ± 0.13 .

We observed a correlation between the changes of R_{Fibre} in the different ROIs and the fibre surface structure with its macroscopic fibrils.

As shown in Fig. 9, the SE images of ROI I exhibited a larger cross section compared to ROIs II and III. In Fig. 9a, the SE image revealed macroscopic fibril orientation with little order on the surface in the ROI I. From Fig. 9, it is also clear that the fibre cross section varies along the longitudinal direction of the fibre. For example, the fibre in ROI II has a smaller cross section than that in ROI I. In ROI II, the macroscopic fibrils are much better aligned than in ROI I, which exists in an ordered, aligned way. Similar observations can be made for ROI III. ROI IV shows a more complex structure of the macro fibrils.

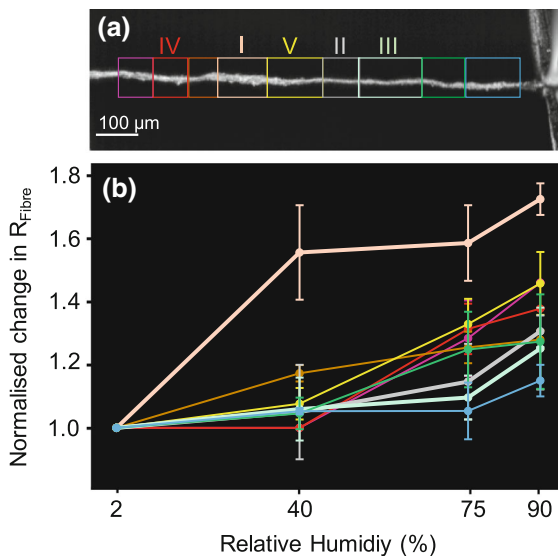
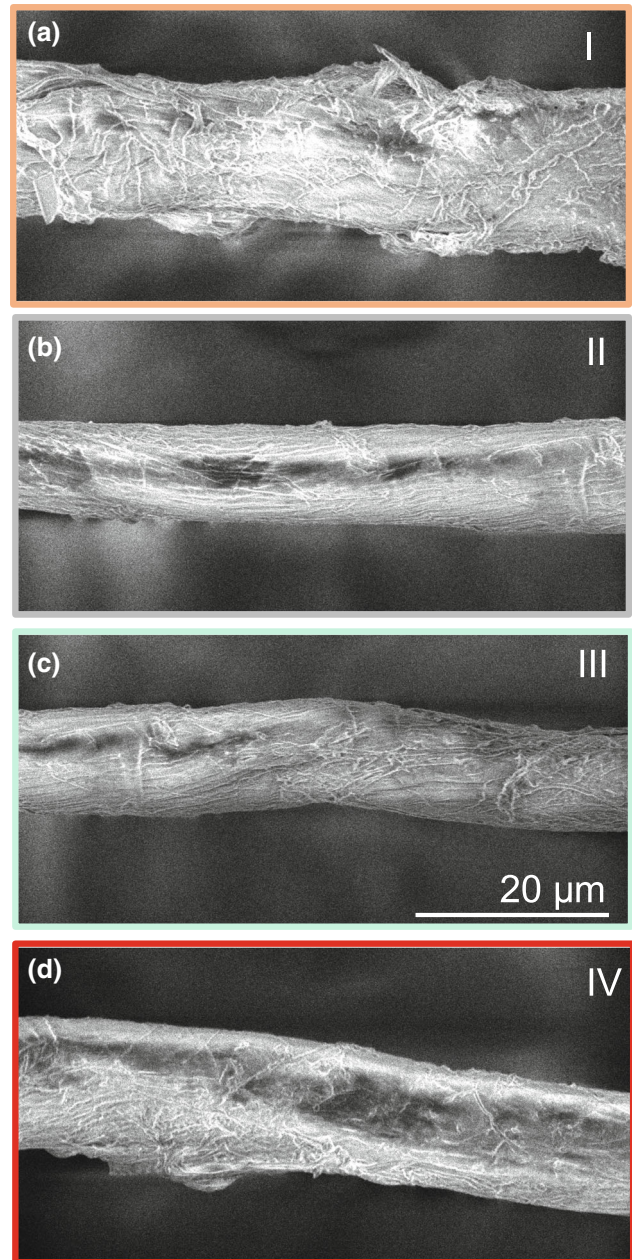


Fig. 8 **a** CLSM microscopy image of the investigated fibre. The coloured boxed indicate the ROIs. **b** The normalised change in $R_{Fibre}/R_{RH=2}$ is displayed over the relative humidity in % of the marked regions of (a)

Colloidal probe mapping

Mechanical properties such as local adhesion, energy dissipation, or the bending of the paper fibre were investigated with AFM. Properties such as contact stress and strain were calculated according to Eqs. 3 and 4. The measurements were carried out with a

Fig. 9 SE images of fibre sections. **a** ROI I, **b** ROI II, **c** ROI III, **d** ROI IV



colloidal probe bending the fibre point by point along the longitudinal direction of the fibre. Thus, a detailed image of the mechanical behaviour along the fibre could be obtained. Mechanical properties such as adhesion, dissipation, and bending ability were estimated from the force-distance data together with contact stress and strain, as displayed in Fig. 10. Figure 10a shows the CLSM together with the mechanical properties at 2% RH, b at 40% RH, c at

75% RH, and d at 90% RH. The shape of the fibre is consistent at all RHs; thus, significant fibre twisting can be excluded.

First, we will discuss the evolution of the adhesion properties with increasing RH. The data in Figs. 10 and 11b and c clearly show that the adhesion force increases with increasing RH. In general, two trends in adhesion changes with increasing RH could be observed: (i) a strong increase in adhesion with

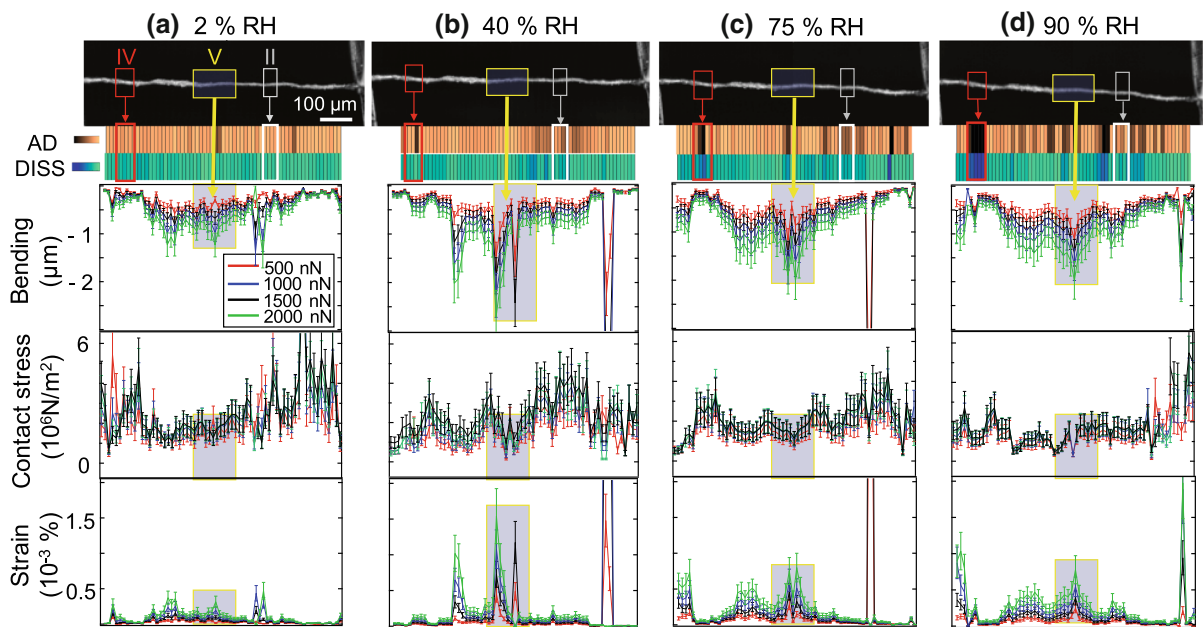


Fig. 10 Mechanical characterisation of a cellulose fibre along the longitudinal direction of the fibre. From top to bottom: CSLM image of the fibre with the local adhesion and dissipation maps along the fibre beneath. The scale bars are -800 to 0 nN (adhesion) and 1 to 1×10^5 J (dissipation). Beneath: bending

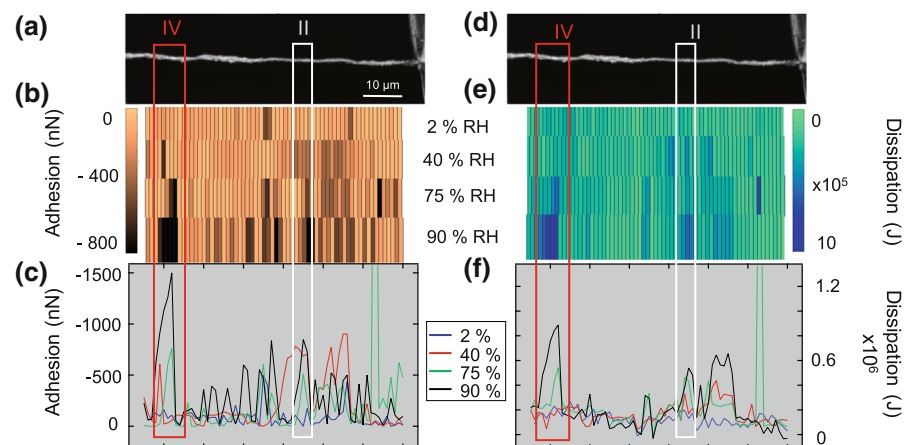
behaviour, contact stress (error 30%) and strain (error 25%) along the fibre. The mechanical properties in **a** are at 2% RH, **b** at 40% RH, **c** 75% RH and **d** 90% RH. The discussed ROIs are marked with II, IV, and V

increasing RH, as observed in ROI IV, and (ii) a minor increase in adhesion, as in ROI II. The corresponding topographies with their macroscopic fibril orientation in both ROIs are shown in the SE images in Fig. 9. Figure 9b) displays the topography of ROI II, which exhibits an ordered macroscopic fibril orientation along the fibre. Figure 9d reveals more macroscopic fibrils oriented on the surface in ROI IV than in ROI II.

From the bending data in Fig. 10, the local bending increased when increasing the RH from 2% RH to 90%. Additionally, mechanical effects (clamping) play a role: the bending of the fibre is reduced at both fixed ends and is increased in the middle of the fibre. Here, the reduced bending at both ends is due to attachment to the sample holder.

An interesting observation is marked in the ROI V in Fig. 10. At 2% RH, the bending behaviour looks

Fig. 11 Adhesion and dissipation maps along the longitudinal direction of the fibre. **a** CLSM image of the fibre, **b** of adhesion maps and **c** corresponding cross-sections along the fibre at different RHs. **d** CLSM image of the fibre (same as a), **(b)** dissipation map and **(c)** corresponding cross sections along the fibre at different RHs



normal with increased bending ability in the middle of the fibre. When increasing the RH to 40%, ROI V exhibited two significant notches at positions where the fibre was particularly soft. The soft regions (notches) broadened and were no longer distinctive at 75% RH. When increasing the RH further to 90%, only one notch (= soft region) could be distinguished. A possible interpretation is that by increasing the RH, more water molecules intrude into the cellulose network, weakening the internal structure (Cabrera et al. 2011; Gumuskaya et al. 2003; John and Thomas 2008), which reduces the stability of the fibre. In addition, the water molecules act as lubricants between the fibrils, which leads to the ability of higher bending at higher RH as the fibrils can slip along each other. As indicated in ROI IV in Fig. 10, some areas exhibit distinctive regions with strong local deformation (notches in the plot). Thus, one might speculate that at 40% RH, “wet spots” develop, which weaken the fibre in distinctive regions. Increasing the RH further to 90% RH, more water molecules diffuse in the other parts of the fibre, which leads to more uniform deformation along the longitudinal direction of the fibre.

In Fig. 12 local bending lines are given for selected forces. The pronounced and repeated bending ability of ROI V is marked in yellow. Also, other features in the bending ability are visible. In the red marked areas in all graphs from Fig. 12 some very pronounced bending features can be observed. These are interpreted to origin from noise from the measurement. As they occur near the fixed end the bending ability of the fibre was actually reduced and the colloidal probe probably slipped along/from the fibre. Overall, Fig. 12 suggests that the reproduceable bending features (yellow) were due to local variations in the fibre properties.

To verify that the bending behaviour displays the actual bending behaviour with its features, we performed a second set of experiments where we characterized a fibre for two RH cycles (see next section).

In the contact stress graphs in Fig. 10, it is evident that the contact stress was higher at both ends of the fibre. This is due to the attachment at the fixed ends and should not be interpreted as a higher strength of the fibre. The contact stress at both fixed ends decreases as the RH is increased. Additionally, here, the increased amount of water molecules inside the

cellulose network destroys bonds and act as a lubricant between the fibrils, which leads to fibre softening.

The strain displayed in Fig. 10 is linked to the bending properties of the fibre. Thus, the strain behaviour follows the same trend as the bending behaviour and is assumed to be interpreted identically.

Furthermore, the applied method makes it possible to establish stress–strain diagrams for each loading point. The stress–strain diagrams for ROIs I, II, and III are displayed in Fig. 13. To derive the stress–strain curves, the stress and strain are also calculated for 200 nN and 350 nN for completeness.

The stress–strain diagram of ROI I is shown in Fig. 13a. It is evident that the slopes in the linear-elastic area decrease with increasing RH. In a linear elastic area, stress and strain are proportional and the deformation is reversible. In a non-linear elastic area, the stress and strain are not proportional to each other, but the deformation is still reversible. In an elastic–plastic area the deformation is partly plastic and irreversible. At 2% and 40% RH, linear-elastic and non-linear elastic areas are monitored but no elastic–plastic areas are detected. At 75% and 90% RH, the non-linear elastic area is distinctively larger than that at 2% and 40% RH. However, there is no clear indication for an elastic–plastic area. Therefore, we suggest that there is no plastic deformation in the fibre structure in ROI I.

Figure 13b shows the stress–strain diagram of ROI II. The slopes in the linear-elastic area also decrease with increasing RH. The non-linear-elastic area increases with increasing RH. Additionally, no clear indication for an elastic–plastic area could be observed.

ROI III, shown in Fig. 13c, exhibited the same behaviour as ROIs I and II. The slopes in the linear-elastic area decreased with increasing RH, and the non-linear-elastic regime increased with increasing RH. Additionally, no clear indication for an elastic–plastic regime can be found within the error bars.

These observations strengthen the assumption that the fibre could fully recover its structure between the static colloidal probe experiments, and our method with applying multiple setpoints could additionally preserve the fibre.

In the supplementary information a chapter of the determination of the virtual Young’s moduli is given.

Fig. 12 Bending along the longitudinal direction of the fibre at different RHs. **a** at 500 nN, **b** at 1000 nN, **c** at 1500 nN and **d** at 2000 nN. The ROI V is marked in yellow. Data close to the fibre attachment (red) can be attributed to experimental noise (probe slippage)

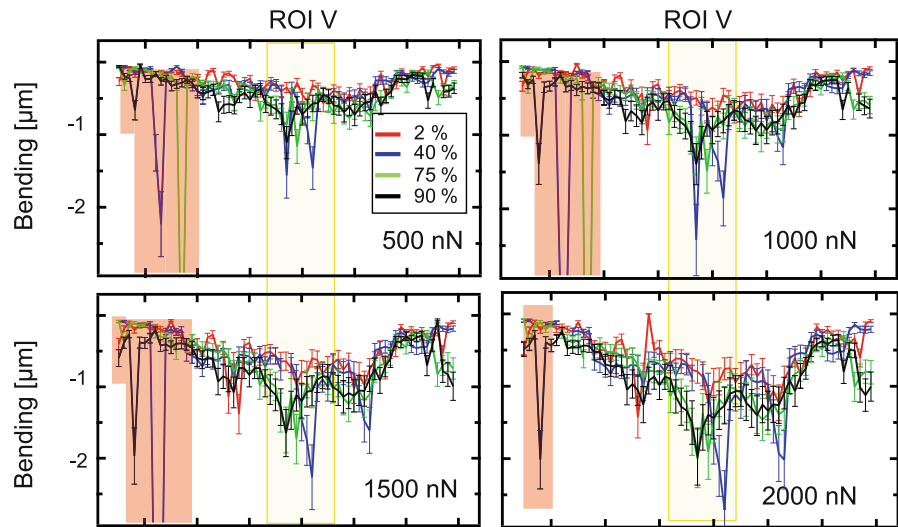
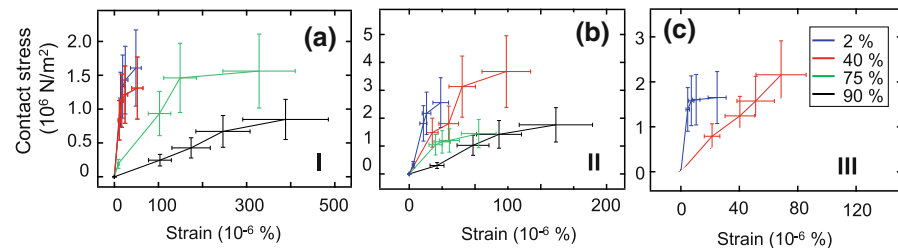


Fig. 13 Stress–strain diagrams of ROI I in (a) of ROI II in (b) and of ROI III in (c)



Repeatability of the measurement

Our measurement technique was applied to another fibre under test for two cycles of changing the RH to detect the possible variations in the change of the normalised R_{Fibre} and in the bending behaviour and to assess the repeatability of the experiments. The first cycle was performed as: every RH firstly measured at the CLSM, moved to the AFM and then increase the RH and move back to the CLSM. Then the fibre was dried for 6 days and a second cycle was performed in the same measurement order as the first cycle. For better visualisation, the 20% error in the bending is not included in the following figures.

In Fig. 14 the normalised R_{Fibre} over the RH for every ROI changes and two different cycles of changing the RH is shown. It is clear that the increase in the normalised R_{Fibre} over the RH for every ROI changes and differs slightly within the two different cycles. This variation between the cycles can be attributed partially to cycle-to-cycle variation of the CLSM experiments due to slightly different loading

points but also to irreversible (or only very slowly reversible) variations of intrafibre properties. We suggest that the increase of RH in the first cycle lead to breaking of internal bonds the cellulose structure did not fully recover and a structural change appeared when the fibre dried. Therefore, the increase of the normalised R_{Fibre} over the RH changed in the second cycle.

In Fig. 15 the adhesion, dissipation and the bending behaviour for both cycles is shown as an overview image. The adhesion and dissipation increased with increasing RH as expected. Apart from that some minor changes can be identified.

To verify the differences in adhesion and dissipation between both cycles, adhesion and dissipation are plotted in Fig. 16. The adhesion properties in both cycles were similar. Some spikes occurred during the first cycle (e.g. at 2% RH), which did not occur in the second cycle. In the dissipation plot it is visible that data of both cycles differs in particular close to the fibre attachment (left side of the graph). These differences could be explained by probe slippage or

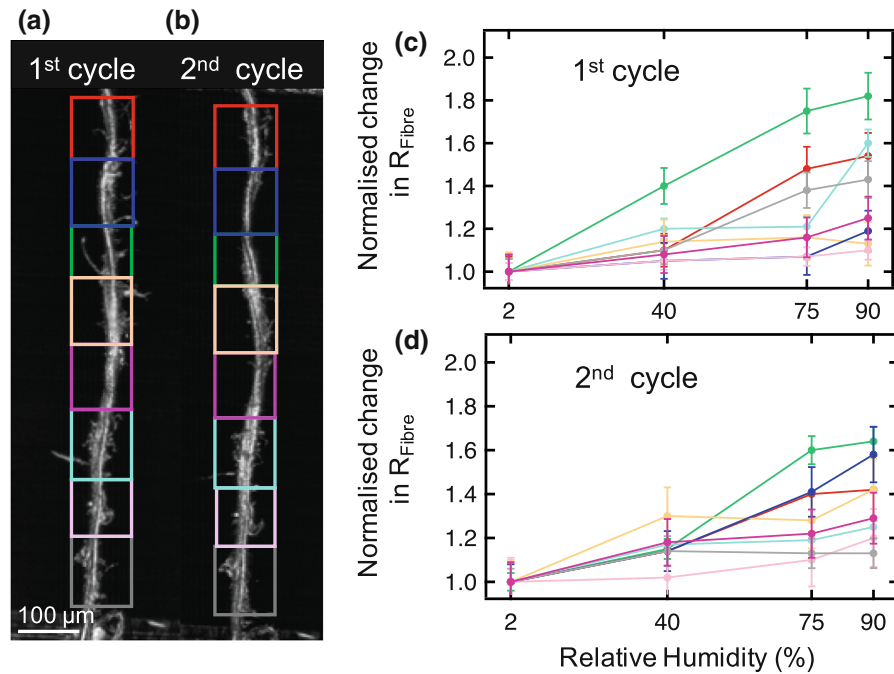


Fig. 14 **a** and **b** displays a CLSM image of the first and second cycle of changing the RH with the respective ROIs of interest. **c** and **d** show the normalised change in R_{Fibre} over the RH for the

first and second cycle of changing the RH (colour coded with respect to the ROI)

twisting of the fibre in between the two cycles. Otherwise, the dissipation properties were similar in both RH cycles.

We divided the adhesion and dissipation properties from the first cycle with them from the second cycle and plotted it in a point-wise coefficient along the longitudinal direction of the fibre. This can be seen in Fig. 17.

The point-wise adhesion or dissipation coefficient should be equal to 1, in an ideal condition. As shown in (Fig. 17a) the point-wise adhesion coefficient showed a high noise ratio in some parts of the fibre. The dissipation point-wise coefficient in (Fig. 17b) also exhibited a high noise ratio in some parts of the fibre, but especially in the beginning of the fibre. This could be attributed to the twisting of the fibre in between the two cycles of RH (see Fig. 14 pink and turquoise ROI). As a cotton linter fibre is a natural occurring and processed material, it cannot be expected to obtain a highly reproducible measurement.

The bending ability is plotted in Figure S8 for both cycles. In cycle #1 the highest applied force of 2000 nN could be reached. The bending ability could be mapped sufficiently for every loading point. As

discussed in the previous section some “soft-spots” can be identified. These soft spots are diminishing with increasing RH.

In cycle 2 the 2000-nN-setpoint could not be reached for almost all loading points at all RH. In addition, some regions can be identified, where the bending could not be mapped in a reliable manner. This implies that with wetting of the fibre or exposing the fibre to humidity, the strength of the fibre could be lost for a time period which is longer than the experiment.

Similar to Figure S7, in Figure S8 the bending ability is plotted for different RHs for both cycles. There it is shown that the soft spots of the fibre are vanishing with increasing RH in the first cycle, but are more distinctive in the second cycle. This also strengthens the assumption that the fibre strength could be lost when exposing the fibre to RH more often.

In this verification experiment, the bending ability of the fibre was decreased at both fixed ends due to clamping. In other regions of the fibre, “soft spots” again developed.

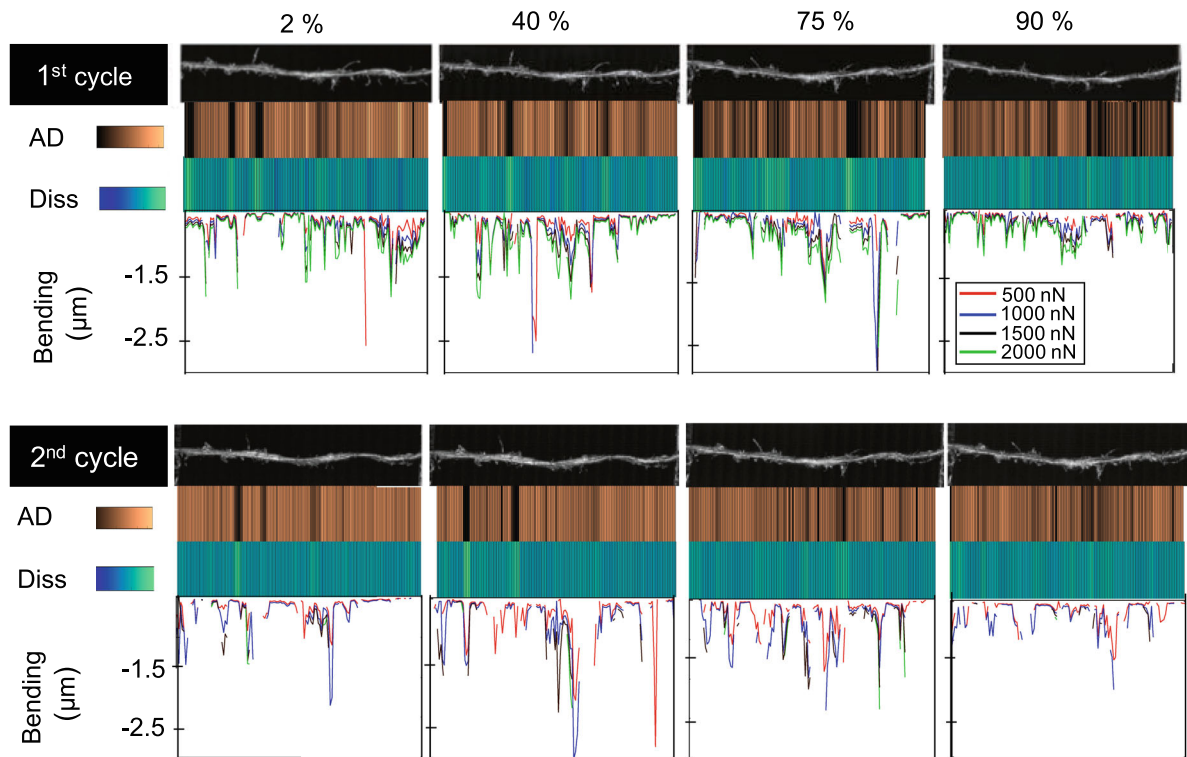


Fig. 15 The CLSM images as well as the mechanical properties such as adhesion, dissipation and the bending abilities for two cycles of changing the RH are shown

Furthermore, Fig. 14 shows that the increase in the normalised R_{Fibre} over the RH for every ROI changes and differs within the two different cycles. In Fig. 17, changes between the two cycles of varying the RH in adhesion and dissipation properties as well as in the bending behaviour (S7 and S8) are observable. In the second cycle of changing the RH, the setpoint of 2000 nN could not be reached in most spots. Thus, it can be suggested that with wetting of the fibre or exposing the fibre to RH, fibre strength is lost.

This fact also highlights the value of our method. By reading out the “virtual setpoint forces” beneath the setpoint, the mechanical properties of the fibre can be displayed at different setpoint forces at a uniform fibre state. Nonlinearities or peculiar effects, such as local softening, can be detected.

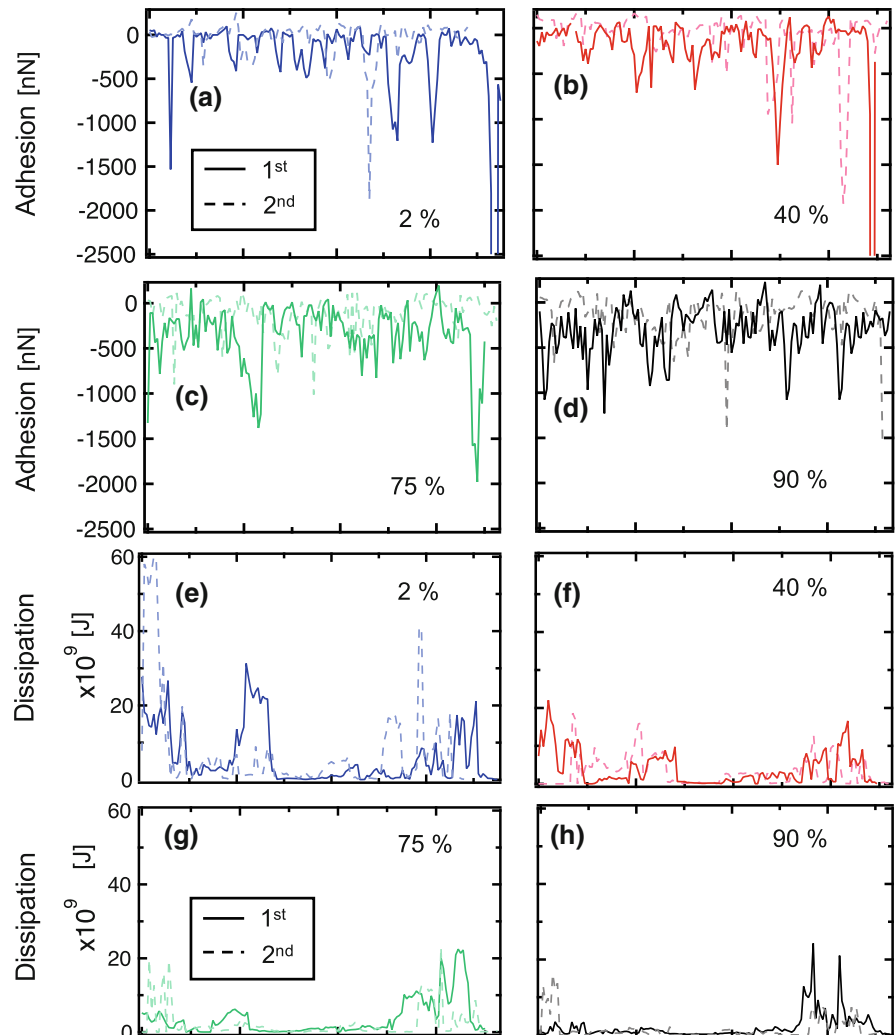
Conclusions

We measured the mechanical properties of a free hanging cotton linter fibre (clamped at both ends) with

colloidal probe AFM along longitudinal direction of the fibre. The proposed method of scanning along the longitudinal direction of the fibre provides a more detailed picture of the mechanical behaviour than conventional three-point bending tests, where only one measurement is performed. To demonstrate the potential of this approach, the mechanical properties of a single cellulose fibre were mapped for varying RH. The colloidal probe data were analysed in correlation with data from CLSM and SEM. The combination of these methods allowed for insights into the interdependence of swelling, bending ability, contact stress, and the stress–strain curves depending on the fibre sections.

With the help of CLSM, the change in the fibre surface curvature radius of different parts of the fibre could be identified. Regions with a lower order in the macroscopic fibril orientation on the surface showed immediate deformation, and regions with a more ordered fibril orientation exhibited steady volume increase.

Fig. 16 a–d Adhesion properties along the longitudinal direction of the fibre of both RH cycles. The 1st cycle is plotted in solid lines and the 2nd cycle in dashed lines. e–h Dissipation properties along the longitudinal direction of the fibre of both RH cycles. The 1st cycle is plotted in solid lines and the 2nd cycle in dashed lines



With the help of force-bending curves obtained with a colloidal probe AFM, it was possible to create a detailed mechanical picture of the paper fibre. Mechanical properties such as adhesion and dissipation, bending ability, contact stress, and strain could be identified. In general, the bending ability increased as RH increased. Additionally, “soft spots” could be identified at an intermediate RH of 40%. Increasing the RH, the soft areas became less distinctive when the entire fibre became softer. This implies that at intermediate RH, individual soft spots can occur in a cotton linter fibre weakening the fibre locally, whereas the entire fibre softens at elevated RH. By analysing the AFM force curves, it was possible to generate stress–strain curves for local points on the fibre. The stress–strain curves were dependent on the

macroscopic fibril orientation: regions with an ordered macroscopic fibril orientation on the surface appeared to be stronger than those with less order. From the stress–strain diagrams, the local Young’s moduli could be identified, and the decrease in values with increasing RH was investigated.

Our approach highlights the difficulties in the three-point bending test, where the fibre is assumed to be homogeneous along the longitudinal direction of the fibre. Mapping with different virtual force setpoints allows one to detect a potentially nonlinear local response of the fibre.

In future work, it will be interesting to address the internal fibre and fibril structure by microtomography or via fluorescent dyes in confocal fluorescence microscopy. Additionally, a better model for the

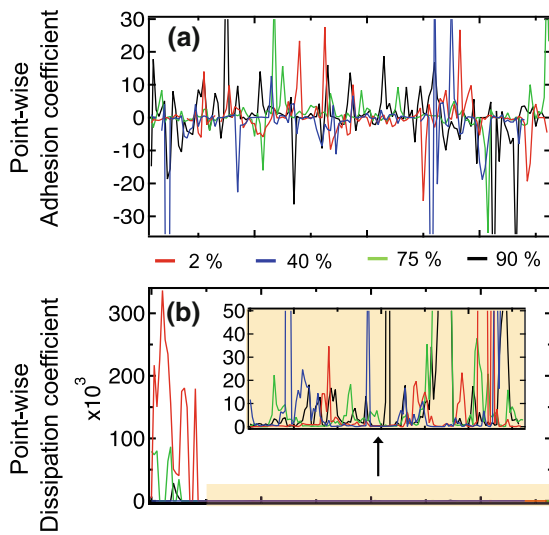


Fig. 17 **a** Point-wise adhesion coefficient: Adhesion of the 1st cycle divided by the 2nd cycle properties along the longitudinal direction of the fibre at the different RHs. **b** Point-wise dissipation coefficient: Dissipation of the 1st cycle divided by the 2nd cycle properties along the longitudinal direction of the fibre at the different

contact area of a colloidal probe and the fibre will be relevant to further develop the method. Thus, better statistics of local mechanical parameters will help to develop computer models of fibres or fibre networks that account for the inhomogeneity of the fibres.

Acknowledgements The authors would like to thank the Deutsche Forschungsgemeinschaft under grant PAK 962 project numbers 405549611, 405422877, 405422473 and 52300548 for financial support. We thank Lars-Oliver Heim for the modification of the cantilever with the colloidal probe.

Author contribution JA wrote the manuscript and conducted all AFM and CLSM measurements and analysis. TK performed the SEM measurements. BL helped with his expertise in Matlab and knowledge about mechanical properties of fibres. J-LS prepared the paper sheets and helped with knowledge about paper fibres. BX, MB and RWS planned and supervised the whole project and are responsible for any correspondence. All authors contributed to the writing of the manuscript.

Funding Open Access funding enabled and organized by Projekt DEAL. The work was supported by Deutsche Forschungsgemeinschaft under grant PAK 962, project numbers 405549611, 405422877, 405422473.

Availability of data and material Additional material is available in the supplementary information.

Code availability The code for contact point calculation is available in the supplementary information.

Declarations

Conflicts of interest The authors have no conflicts of interest to declare that are relevant to the content of this article.

Human and animal rights This is not research involving Human participants and Animals.

Open Access This article is licensed under a Creative Commons Attribution 4.0 International License, which permits use, sharing, adaptation, distribution and reproduction in any medium or format, as long as you give appropriate credit to the original author(s) and the source, provide a link to the Creative Commons licence, and indicate if changes were made. The images or other third party material in this article are included in the article's Creative Commons licence, unless indicated otherwise in a credit line to the material. If material is not included in the article's Creative Commons licence and your intended use is not permitted by statutory regulation or exceeds the permitted use, you will need to obtain permission directly from the copyright holder. To view a copy of this licence, visit <http://creativecommons.org/licenses/by/4.0/>.

References

- Arlov APFO, Mason SG (1958) Particle motions in sheared suspensions. *Sven Papperstidn-Nord Cellul* 61:61–67
- Auernhammer J et al (2021) Nanomechanical characterisation of a water-repelling terpolymer coating of cellulosic fibres. *Cellulose*. <https://doi.org/10.1007/s10570-020-03675-9>
- AZoMaterials (2020) Silica - Silicon Dioxide (SiO₂). <https://www.azom.com/properties.aspx?ArticleID=1114> 9 November 2020
- Barber JR, Barber AK (2018) *Contact Mechanics, Solid Mechanics and Its Applications*. Springer International Publishing, Switzerland. <https://doi.org/10.1007/978-3-319-70939-0>
- Benitez R, Moreno-flores S, Bolos VJ, Toca-Herrera JL (2013) A new automatic contact point detection algorithm for AFM force curves. *Microsc Res Tech* 76:870–876. <https://doi.org/10.1002/jemt.22241>
- Biswas S, Ahsan Q, Cenna A, Hasan M, Hassan A (2013) Physical and Mechanical Properties of Jute Bamboo and Coir Natural. *Fiber Fiber Polym* 14:1762–1767. <https://doi.org/10.1007/s12221-013-1762-3>
- Bump S et al (2015) Spatial, spectral, radiometric, and temporal analysis of polymer-modified paper substrates using fluorescence microscopy. *Cellulose* 22:73–88. <https://doi.org/10.1007/s10570-014-0499-5>
- Buschlediller G, Zeronian SH (1992) Enhancing the reactivity and strength of cotton fibres. *J Appl Polym Sci* 45:967–979. <https://doi.org/10.1002/app.1992.070450604>

- Butt HJ, Jaschke M (1995) Calculation of thermal noise in atomic-force microscopy. *Nanotechnology* 6:1–7. <https://doi.org/10.1088/0957-4484/6/1/001>
- Cabrera RQ, Meersman F, McMillan PF, Dmitriev V (2011) Nanomechanical and structural properties of native cellulose under compressive stress. *Biomacromol* 12:2178–2183. <https://doi.org/10.1021/bm200253h>
- Chard JM, Creech G, Jesson DA, Smith PA (2013) Green composites: sustainability and mechanical performance. *Plast Rubber Compos* 42:421–426. <https://doi.org/10.1179/1743289812y.0000000041>
- Czibula C, Ganser C, Seidlhofer T, Teichert C, Hirn U (2019) Transverse viscoelastic properties of pulp fibers investigated with an atomic force microscopy method. *J Mater Sci* 54:11448–11461. <https://doi.org/10.1007/s10853-019-03707-1>
- Delaney JL, Hogan CF, Tian JF, Shen W (2011) Electrogenenerated Chemiluminescence detection in paper-based microfluidic sensors. *Anal Chem* 83:1300–1306. <https://doi.org/10.1021/ac102392t>
- Derjaguin BV, Muller VM, Toporov YP (1975) Effect of contact deformations on adhesion of particles. *J Colloid Interface Sci* 53:314–326. [https://doi.org/10.1016/0021-9797\(75\)90018-1](https://doi.org/10.1016/0021-9797(75)90018-1)
- El Seoud OA, Fidale LC, Ruiz N, D'Almeida MLO, Frollini E (2008) Cellulose swelling by protic solvents: which properties of the biopolymer and the solvent matter? *Cellulose* 15:371–392. <https://doi.org/10.1007/s10570-007-9189-x>
- Elsayad K et al (2020) Mechanical properties of cellulose fibers measured by brillouin spectroscopy. *Cellulose* 27:4209–4220. <https://doi.org/10.1007/s10570-020-03075-z>
- Fernando S, Mallinson CF, Phanopolous C, Jesson DA, Watts JF (2017) Mechanical characterisation of fibres for engineered wood products: a scanning force microscopy study. *J Mater Sci* 52:5072–5082. <https://doi.org/10.1007/s10853-016-0744-4>
- Fidale LC, Ruiz N, Heinze T, El Seoud OA (2008) Cellulose swelling by aprotic and protic solvents: what are the similarities and differences? *Macromol Chem Phys* 209:1240–1254. <https://doi.org/10.1002/macp.200800021>
- Forgacs OLRA, Mason SG (1958) The hydrodynamic behaviour of paper-making fibres. *Fundam of Papermak Fibres* 59:117–128
- Ganser C, Kreiml P, Morak R, Weber F, Paris O, Schennach R, Teichert C (2015) The effects of water uptake on mechanical properties of viscose fibers. *Cellulose* 22:2777–2786. <https://doi.org/10.1007/s10570-015-0666-3>
- Gavara N (2016) Combined strategies for optimal detection of the contact point in AFM force-indentation curves obtained on thin samples and adherent cells. *Sci Rep* 6:13. <https://doi.org/10.1038/srep21267>
- Groom L, Mott L, Shaler S (2002) Mechanical properties of individual southern pine fibers. Part I determination and variability of stress-strain curves with respect to tree height and juvenility. *Wood Fiber Sci* 34:14–27
- Gumuskaya E, Usta M, Kirci H (2003) The effects of various pulping conditions on crystalline structure of cellulose in cotton linters. *Polym Degrad Stabil* 81:559–564. [https://doi.org/10.1016/S0141-3910\(03\)00157-5](https://doi.org/10.1016/S0141-3910(03)00157-5)
- Hayes RA, Feenstra BJ (2003) Video-speed electronic paper based on electrowetting. *Nature* 425:383–385. <https://doi.org/10.1038/nature01988>
- Hellwig J, Karlsson RMP, Wagberg L, Pettersson T (2017) Measuring elasticity of wet cellulose beads with an AFM colloidal probe using a linearized DMT model. *Anal Methods* 9:4019–4022. <https://doi.org/10.1039/c7ay01219e>
- Hellwig J, Duran VL, Pettersson T (2018) Measuring elasticity of wet cellulose fibres with AFM using indentation and a linearized hertz model anal. *Methods* 10:5. <https://doi.org/10.1039/c8ay00816g>
- Jajcinovic M, Fischer WJ, Mautner A, Bauer W, Hirn U (2018) Influence of relative humidity on the strength of hardwood and softwood pulp fibres and fibre to fibre joints. *Cellulose* 25:2681–2690
- Jayne BA (1959) *Mechanische Eigenschaften Von Holzfasern*. *Tappi J* 42:416–467
- John MJ, Thomas S (2008) Biofibres and biocomposites. *Carbohydr Polym* 71:343–364. <https://doi.org/10.1016/j.carbpol.2007.05.040>
- Liana DD, Raguse B, Gooding JJ, Chow E (2012) Recent advances in paper-based sensors. *Sensors* 12:11505–11526. <https://doi.org/10.3390/s120911505>
- Lin B (2020) Humidity Influence on Mechanics and Failure of Paper Materials: Joint Numerical and Experimental Study on Fiber and Fiber Network Scale arXiv submit/3516584 identifier 2012.08597
- Lin DC, Dimitriadis EK, Horkay F (2007) Robust strategies for automated AFM force curve analysis - I. Non-Adhesive Indentation of Soft, Inhomogeneous Materials *J Biomech Eng-Trans ASME* 129:430–440. <https://doi.org/10.1115/1.2720924>
- Lorbach C, Fischer WJ, Gregorova A, Hirn U, Bauer W (2014) Pulp Fiber Bending Stiffness in Wet and Dry State Measured from Moment of Inertia and Modulus of Elasticity. *BioResources* 9:5511–5528
- Mantanis GI, Young RA, Rowell RM (1995) Swelling of compressed cellulose fibre webs in organic liquids. *Cellulose* 2:1–22
- Mather RR, Wardman RH (2015) *The chemistry of textile fibres*. Royal Society of Chemistry
- Müssig J (2010) *Industrial application of natural fibres*. Wiley, Chichester, West Sussex, U.K.
- Navaranjan N, Blaikie RJ, Parbhu AN, Richardson JD, Dickson AR (2008) Atomic force microscopy for the measurement of flexibility of single softwood pulp fibres. *J Mater Sci* 43:4323–4329. <https://doi.org/10.1007/s10853-008-2636-8>
- Page DH, Elhosseiny F, Winkler K, Lancaster APS (1977) Elastic-Modulus of Sible Wood Pulp Fibres *Tappi* 60:114–117
- Persson BNJ, Ganser C, Schmied F, Teichert C, Schennach R, Gilli E, Hirn U (2013) Adhesion of Cellulose Fibers in Paper *Journal of Physics-Condensed Matter* 25:11. <https://doi.org/10.1088/0953-8984/25/4/045002>
- Pettersson T, Hellwig J, Gustafsson PJ, Stenstrom S (2017) Measurement of the flexibility of wet cellulose fibres using atomic force microscopy. *Cellulose* 24:4139–4149. <https://doi.org/10.1007/s10570-017-1407-6>

- Placet V, Cisse O, Boubakar ML (2012) Influence of environmental relative humidity on the tensile and rotational behaviour of hemp fibres. *J Mater Sci* 47:3435–3446. <https://doi.org/10.1007/s10853-011-6191-3>
- Rudoy D, Yuen SG, Howe RD, Wolfe PJ (2010) Bayesian change-point analysis for atomic force microscopy and soft material indentation *J R Stat Soc Ser C-Appl. Stat* 59:573–593
- Ruettiger C et al (2016) Redox-Mediated Flux Control in Functional Paper *Polymer* 98:429–436. <https://doi.org/10.1016/j.polymer.2016.01.065>
- Salmen NL, Back EL (1980) Moisture-dependent thermal softening of paper, evaluated by its elastic-modulus *Tappi* 63:117–120
- Samuelsson LG (1963) Measurement of the stiffness of fibres. *Sven Papperstidn-Nord Cellul* 66:541–546
- Schmied FJ, Teichert C, Kappel L, Hirn U, Schennach R (2012) Joint strength measurements of individual fiber-fiber bonds: An atomic force microscopy based method. *Rev Sci Instrum* 83:8. <https://doi.org/10.1063/1.4731010>
- Schmied FJ, Teichert C, Kappel L, Hirn U, Bauer W, Schennach R (2013) What holds paper together: Nanometre scale exploration of bonding between paper fibres *Sci Rep* 3 doi:ARTN 243210.1038/srep02432
- Schniewind AP, Ifju G, Brink DL (1966) Effect of drying on the flexural rigidity of single fibres. *Consolidation of the Paper Web* 1:538–543
- Yan DB, Li KC (2008) Wet fiber shear flexibility and its contribution to the overall transverse deformation of fibers. *J Mater Sci* 43:7210–7218. <https://doi.org/10.1007/s10853-008-2958-6>
- Young RA, Rowell RM (1986) *Cellulose : structure, modification and hydrolysis*. New York u.a.

Publisher's Note Springer Nature remains neutral with regard to jurisdictional claims in published maps and institutional affiliations.